Comparison of Droop Control and Virtual Oscillator Control Realized by Andronov-Hopf Dynamics

Minghui Lu*, Victor Purba†, Sairaj Dhople†, Brian Johnson*
*Department of Electrical and Computer Engineering, University of Washington, Seattle, WA 98195
†Department of Electrical and Computer Engineering, University of Minnesota, Minneapolis, MN 55455
Emails: {mhlu, brianbj}@uw.edu, and {purba002, sdhople}@umn.edu

***Abstract*—Virtual oscillator control (VOC) is a time-domain strategy for regulating the operation of grid-forming (GFM) inverters. The premise of this method is to leverage the dynamics of nonlinear oscillator circuits to realize controllers; the time-domain nature of the resulting implementation is starkly different from classical droop control methods. This paper considers VOC realized with the dynamics of the Andronov-Hopf oscillator, a second-order nonlinear dynamical system that enables GFM inverters to be dispatched and generate low-harmonic outputs while not compromising dynamic performance. Leveraging an equilibrium analysis of the involved dynamics and small-signal models, we put forth a side-by-side comparison of dynamic performance and small-signal stability with classical droop control. The results demonstrate superior dynamic performance of VOC, and broadly, the paper furthers efforts focused on modeling and analysis of this general class of GFM controllers.**

I. Introduction

Inverter controllers that are capable of sustaining system frequency and voltage profile in the absence of conventional fossil-fuel-powered generation have found significant recent interest given the accelerating rate at which renewables continue to be deployed. This class of controllers is often referred to as *grid-forming* (GFM), since it allows for the realization of power grids with decentralized primary control and power sharing—features that are commonplace with synchronous-generator based systems today. In this paper, we focus on a GFM controller that is built around a second-order nonlinear dynamical system called the Andronov-Hopf oscillator (AHO) [1], [2]. This admits a nonlinear circuit realization, and in fact, is one of many that have been proposed recently to realize GFM controllers under the so-called Virtual Oscillator Controller (VOC) paradigm [3]–[5]. (Other notable instances include Van der Pol [6] and Dead-zone [7] circuits.) We compare the dynamic performance of the AHO-based GFM controller with the classical droop control method [8]–[10] after formulating small-signal models for each control type. By uncovering the impact of intrinsic physical attributes, control parameters, and external inputs on system stability and dynamic performance, this analysis advances the state-of-the-art in modeling and design of GFM inverter systems.

This material is based upon work supported by the U.S. Department of Energy's Office of Energy Efficiency and Renewable Energy (EERE) under Solar Energy Technologies Office (SETO) Agreement Number EE0009025, the National Science Foundation through grant 1509277, and Washington Research Foundation.

Droop control is widely recognized as the default control strategy for GFM inverters. Of relevance to the line of work in this paper, there are several noteworthy efforts in large- and small-signal models for droop control [11], [12] and associated system-design considerations [13], [14]. Interestingly, VOC-based controllers can be engineered for droop-like behavior in steady state with (close to) linear trade-offs in active-power versus frequency and reactive-power versus voltage [15], [16]. On the other hand, the real-time behavior of VOC is fundamentally different since it is engineered from dynamics that are innately nonlinear and implemented entirely in the time domain. It is, in fact, this time-domain nature of VOC-based controllers that enables swift responses of the corresponding GFM inverters in the face of disturbances. Previous efforts have compared dynamic performance of VOC realized with Van der Pol oscillator dynamics and droop control with appropriate small-signal models [17]. This work provides a meaningful extension to such comparative studies by examining VOC realized with AHO dynamics alongside droop control. Compared to other VOC implementations based on, e.g., Van der Pol oscillators, AHO-based VOC implementations offer better harmonic performance and they can be dispatched, in the sense that their nominal active and reactive-power outputs are easily tunable. Therefore, they have been the subject of several recent investigations [18]–[20], further justifying the focus of this effort.

Our setup consists of a three-phase GFM inverter connected to an external network through an inductive filter. We begin by discussing the nonlinear dynamical models for the AHO-based VOC controller and an equivalent droop implementation. Following this, we precisely uncover the equilibria corresponding to the dynamical models for each controller type and analytically establish corresponding small-signal models in each case. With these models in place, we undertake a variety of numerical simulations. First, for a nominal set of design parameters for which the steady-state droop behavior of both control strategies match, we illustrate that the AHO-based controller offers a superior dynamic response due to its speed and no overshoot. Next, we investigate the impact of: i) the R/L ratio corresponding to the output filter (and interconnecting transmission lines), and ii) active-power setpoint on eigenvalues of the linearized models. Finally, our small-signal models are validated with nonlinear simulations.

The remainder of this paper is organized as follows: In

978-1-7281-5414-5/20/$31.00 ©2020 IEEE

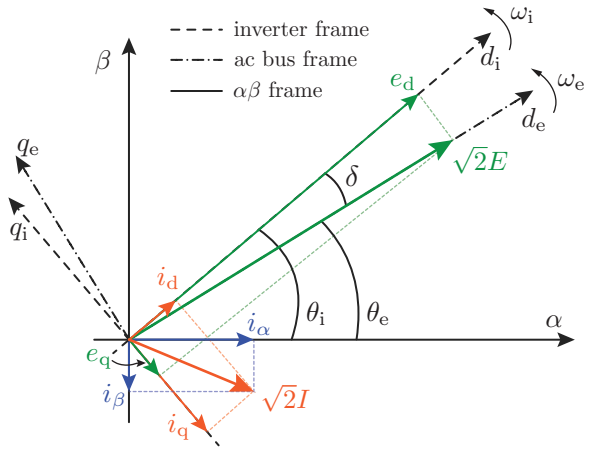

Figure 1: Illustrating frequently referenced voltage and current signals in pertinent reference frames.

Section II, we overview modeling preliminaries and the dynamic models for AHO and droop control. Section III presents the equilibria and small-signal models for each controller. Numerical simulations follow in Section IV, and we conclude the paper in Section V with a few directions for future work.

II. Preliminaries and GFM Controller Models

In this section, we first discuss mathematical and modeling preliminaries. Next, we overview the dynamic models for the two GFM controllers.

A. Preliminaries

The system under study is a three-phase GFM voltage-source inverter (VSI). The inverter includes a dc voltage source, v_dc, a hex-bridge converter, and an output inductive filter with inductance L_f and resistance R_f (these may also include line impedances, if any). Recall that the two GFM strategies we examine are VOC realized with the dynamics of an Andronov-Hopf Oscillator and droop control. The system architectures with these control types are depicted in Figs. 2(a) and 2(b), respectively. The three-phase voltages corresponding to the external network and the inverter terminals are denoted by e_abc and v_abc, respectively. In the $\alpha\beta$ reference frame, we can represent the network and inverter-terminal voltages as:

$$\begin{cases} e_\alpha = \sqrt{2}E\cos\omega_\mathrm{e}t \\ e_\beta = \sqrt{2}E\sin\omega_\mathrm{e}t, \end{cases} \qquad \begin{cases} v_\alpha = \sqrt{2}V\cos\omega_\mathrm{i}t \\ v_\beta = \sqrt{2}V\sin\omega_\mathrm{i}t. \end{cases} \tag{1}$$

Implicit in the definitions above is that the amplitudes of the two voltages are denoted by $\sqrt{2}E$, $\sqrt{2}V$; and frequencies are denoted by ω_e, ω_i. In what follows, we will also find it useful to define corresponding voltage phase angles by $\theta_\mathrm{e} = \omega_\mathrm{e}t$, $\theta_\mathrm{i} = \omega_\mathrm{i}t$, respectively. To facilitate analysis, we will reference the angle difference $\delta = \theta_\mathrm{i} - \theta_\mathrm{e}$ in subsequent developments. The inverter output currents (referred interchangeably as line currents) in the $\alpha\beta$ reference frame are denoted by i_α, i_β, respectively, and in the local dq reference frame by $i_\mathrm{d}, i_\mathrm{q}$, respectively. The dynamics of i_d and i_q are given by [21]

$$\begin{bmatrix} \dot{i}_\mathrm{d} \\ \dot{i}_\mathrm{q} \end{bmatrix} = \begin{bmatrix} -\frac{R_\mathrm{f}}{L_\mathrm{f}} & \omega_\mathrm{i} \\ -\omega_\mathrm{i} & -\frac{R_\mathrm{f}}{L_\mathrm{f}} \end{bmatrix} \begin{bmatrix} i_\mathrm{d} \\ i_\mathrm{q} \end{bmatrix} + \frac{1}{L_\mathrm{f}} \begin{bmatrix} \sqrt{2}V - e_\mathrm{d} \\ 0 - e_\mathrm{q} \end{bmatrix}, \tag{2}$$

where $e_\mathrm{d}, e_\mathrm{q}$ correspond to the dq reference-frame representations of the external network voltage. Given the definitions and notation above, we can express:

$$\begin{bmatrix} e_\mathrm{d} \\ e_\mathrm{q} \end{bmatrix} = \begin{bmatrix} \cos\delta & \sin\delta \\ -\sin\delta & \cos\delta \end{bmatrix} \begin{bmatrix} \sqrt{2}E \\ 0 \end{bmatrix}. \tag{3}$$

The instantaneous active and reactive power at the inverter terminals are denoted by P and Q, and they are defined as

$$P = \frac{3}{2}\sqrt{2}Vi_\mathrm{d}, \quad Q = -\frac{3}{2}\sqrt{2}Vi_\mathrm{q}. \tag{4}$$

Figure 1 illustrates several of the quantities referenced above.

B. AHO Controller

The AHO controller, depicted in Fig. 2(a), is composed of three main parts. First is a resonant LC tank with natural frequency $\omega_\mathrm{nom} = 1/\sqrt{LC}$, characteristic impedance $\varepsilon = \sqrt{L/C}$, and corresponding state variables $[v_\mathrm{C}, i_\mathrm{L}]^\top$. Next, there are two negative conductances $-\sigma$ and $-\varepsilon^2\sigma$ which systematically inject energy into the circuit to sustain oscillations. Finally, we have nonlinear state-dependent voltage and current sources, denoted by $g_\mathrm{v} := \varepsilon\alpha(v_\mathrm{C}^2 + \varepsilon^2 i_\mathrm{L}^2)\varepsilon i_\mathrm{L}$ and $g_\mathrm{i} := \alpha(v_\mathrm{C}^2 + \varepsilon^2 i_\mathrm{L}^2)v_\mathrm{C}$, respectively.

A detailed description of the system dynamical model and design strategy are available in [2]. In what follows, we provide a broad overview pertinent to the comparative analysis with droop control. The differential equations that govern the evolution of v_C and i_L are given by

$$C\dot{v}_\mathrm{C} = -i_\mathrm{L} - g_\mathrm{i} + \sigma v_\mathrm{C} - u_1, \tag{5a}$$

$$L\dot{i}_\mathrm{L} = v_\mathrm{C} - g_\mathrm{v} + \sigma\varepsilon(\varepsilon i_\mathrm{L}) - \varepsilon u_2, \tag{5b}$$

where u_1, u_2 are derived from the difference between measured line currents and setpoints in the $\alpha\beta$ domain:

$$\begin{bmatrix} u_1 \\ u_2 \end{bmatrix} = \kappa_\mathrm{i} \underbrace{\begin{bmatrix} \cos\varphi & -\sin\varphi \\ \sin\varphi & \cos\varphi \end{bmatrix}}_{=:R(\varphi)} \begin{bmatrix} i_\alpha - i_\alpha^\star \\ i_\beta - i_\beta^\star \end{bmatrix}. \tag{6}$$

The rotation matrix referenced above, $R(\varphi)$, facilitates tuning the steady-state droop laws; with the value $\varphi = \pi/2$, we obtain voltage reactive-power and frequency active-power trade-offs. The constant κ_i is a current-scaling gain. The PWM modulation signals, v_α, v_β are obtained by scaling v_C and εi_L by the fixed gain κ_v. The voltage dynamics follow as

$$\begin{bmatrix} \dot{v}_\alpha \\ \dot{v}_\beta \end{bmatrix} = \begin{bmatrix} \frac{\xi}{\kappa_\mathrm{v}^2}\left(2V_\mathrm{nom}^2 - V^2\right) & -\omega_\mathrm{nom} \\ \omega_\mathrm{nom} & \frac{\xi}{\kappa_\mathrm{v}^2}\left(2V_\mathrm{nom}^2 - V^2\right) \end{bmatrix} \begin{bmatrix} v_\alpha \\ v_\beta \end{bmatrix} - \frac{\kappa_\mathrm{v}}{C}\kappa_\mathrm{i} R(\varphi) \begin{bmatrix} i_\alpha - i_\alpha^\star \\ i_\beta - i_\beta^\star \end{bmatrix}, \tag{7}$$

where $\sqrt{2}V := (v_\alpha^2 + v_\beta^2)^{\frac{1}{2}}$ (thereby rendering the above model to be nonlinear), $V_\mathrm{nom} := \sqrt{\sigma\kappa_\mathrm{v}^2/(2\alpha)}$ is the nominal inverter voltage setpoint, and $\xi := \alpha/C$ is a gain which influences convergence speed. The dynamics in (7) can be written in

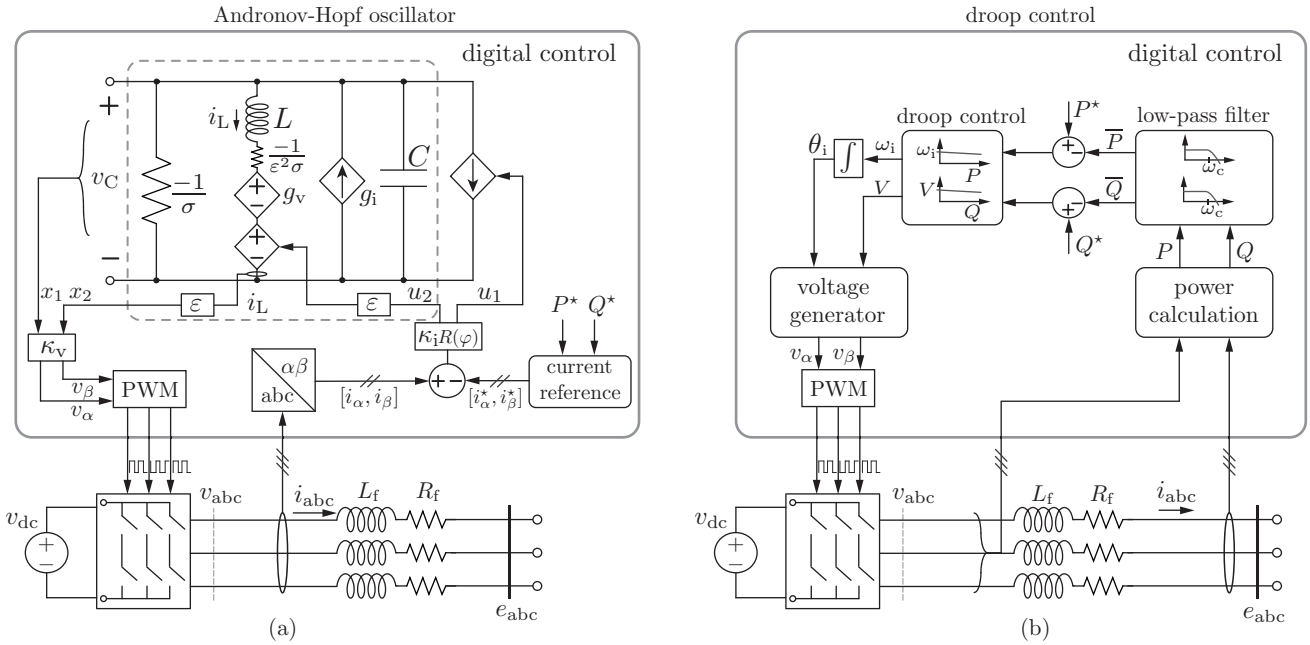

Figure 2: Voltage source inverter with (a) Andronov-Hopf oscillator controller (inset with dashed box), (b) droop controller. In (a), the current setpoints are obtained from the active- and reactive-power setpoints by solving algebraic equations housed in the "current reference" block (these equations are similar to (4)). In (b), the "power calculation" block calculates the active- and reactive-power using (4), the "low-pass filter" block comprises two low-pass filters with cutoff frequency of $\omega_{\rm c}$, the "droop control" block denotes the droop relationships given in (10), and the "voltage generator" block generates the PWM modulation signals in the $\alpha\beta$ reference frame given corresponding polar-coordinate inputs.

polar coordinates, i.e., with voltage V and angle $\theta_{\rm i}$ as states, in the following manner:

$$\dot{V} = \frac{\xi}{\kappa_{\rm v}^2} V\left(2V_{\rm nom}^2 - 2V^2\right) - \frac{\kappa_{\rm v}\kappa_{\rm i}}{3CV}(Q - Q^\star), \tag{8a}$$

$$\dot{\theta}_{\rm i} = \omega_{\rm i} = \omega_{\rm nom} - \frac{\kappa_{\rm v}\kappa_{\rm i}}{3CV^2}(P - P^\star), \tag{8b}$$

where $P^\star, Q^\star$ denote the active- and reactive-power setpoints, and P, Q denote the active- and reactive-power outputs measured at the inverter terminals (4). The setpoints bias droop behavior, and there is flexibility in their choice with the constraint that they should adhere to the inverter apparent-power rating. The phase dynamics can be equivalently expressed with the power angle δ as follows

$$\dot{\delta} = \omega_{\rm nom} - \omega_{\rm e} - \frac{\kappa_{\rm v}\kappa_{\rm i}}{3CV^2}(P - P^\star). \tag{9}$$

C. Droop Controller

The implementation of droop control is depicted in Fig. 2(b). At the core are the following linear trade-offs:

$$V = V_{\rm nom} - m_{\rm q}(\overline{Q} - Q^\star), \tag{10a}$$

$$\omega_{\rm i} = \omega_{\rm nom} - m_{\rm p}(\overline{P} - P^\star), \tag{10b}$$

where $\overline{P}, \overline{Q}$ are filtered active- and reactive-power values measured at the inverter terminals (we discuss this shortly), and $m_{\rm q}, m_{\rm p}$ are determined by the voltage- and frequency-droop specifications. For instance, if we assume a 5% voltage droop and $0.5\,$Hz frequency droop while the inverters are running at rated power $S_{\rm rated}$, then it follows that $m_{\rm q} = 0.05V_{\rm nom}/S_{\rm rated}$ and $m_{\rm p} = 2\pi 0.5\,{\rm Hz}/S_{\rm rated}$. To reject double-frequency pulsating components that arise from imbalances and switching ripple (which are inescapable in practical systems) from the power calculations, a low-pass (LP) filter is required. In this paper, we adopt a first-order LP filter, although, the analysis presented readily generalizes to other filters. The dynamics of the filtered active- and reactive-power, denoted by $\overline{P}$ and $\overline{Q}$, respectively, can be written as

$$\dot{\overline{P}} = \omega_{\rm c}(\overline{P} - P), \quad \dot{\overline{Q}} = \omega_{\rm c}(\overline{Q} - Q), \tag{11}$$

where $\omega_{\rm c}$ is the cut-off frequency which typically ranges from several Hz to tens of Hz. In general, the LP filter will hinder control responsiveness as the filtered quantities are leveraged inside the droop controller. Therefore, the selection of the cut-off frequency, $\omega_{\rm c}$, is an important design choice and it presents an important trade-off between power-filtering performance and system-transient response.

The dynamics of the terminal voltage amplitude V and angle $\theta_{\rm i}$ in (10) are given by:

$$\dot{V} = -m_{\rm q}\dot{\overline{Q}} = m_{\rm q}\omega_{\rm c}(\overline{Q} - Q^\star), \tag{12a}$$

$$\dot{\theta}_{\rm i} = \omega_{\rm nom} - m_{\rm p}(\overline{P} - P^\star). \tag{12b}$$

As with the AHO controller, we will find it useful to express the phase dynamics with the power angle δ as follows

$$\dot{\delta} = \omega_{\rm nom} - \omega_{\rm e} - m_{\rm p}(\overline{P} - P^\star). \tag{13}$$

III. Equilibria and Small-signal Models

In this section, we derive the steady-state equilibria corresponding to the system dynamical models composed of the

TABLE I
SMALL-SIGNAL MODELS FOR AHO AND DROOP CONTROL.

	Jacobian matrix, A
AHO	$\begin{bmatrix} 0 & \frac{\kappa_\mathrm{v}\kappa_\mathrm{i} i_{\mathrm{d,eq}}}{\sqrt{2}CV_\mathrm{eq}^2} - \frac{2\kappa_\mathrm{v}\kappa_\mathrm{i}P^\star}{3CV_\mathrm{eq}^3} & -\frac{\kappa_\mathrm{v}\kappa_\mathrm{i}}{\sqrt{2}CV_\mathrm{eq}} & 0 \\ 0 & \frac{\xi}{\kappa_\mathrm{v}^2}(2V_\mathrm{nom}^2 - 6V_\mathrm{eq}^2) - \frac{\kappa_\mathrm{v}\kappa_\mathrm{i}Q^\star}{3CV_\mathrm{eq}^2} & 0 & \frac{\kappa_\mathrm{v}\kappa_\mathrm{i}}{\sqrt{2}C} \\ \frac{\sqrt{2}E\sin\delta_\mathrm{eq}}{L_\mathrm{f}} & \frac{\kappa_\mathrm{v}\kappa_\mathrm{i} i_{\mathrm{d,eq}} i_{\mathrm{q,eq}}}{\sqrt{2}CV_\mathrm{eq}^2} - \frac{2\kappa_\mathrm{v}\kappa_\mathrm{i} i_{\mathrm{d,eq}}P^\star}{3CV_\mathrm{eq}^3} + \frac{\sqrt{2}}{L_\mathrm{f}} & -\frac{R_\mathrm{f}}{L_\mathrm{f}} - \frac{\kappa_\mathrm{v}\kappa_\mathrm{i} i_{\mathrm{q,eq}}}{\sqrt{2}CV_\mathrm{eq}} & \omega_\mathrm{nom} - \frac{k_\mathrm{v}k_\mathrm{i} i_{\mathrm{d,eq}}}{\sqrt{2}CV_\mathrm{eq}} + \frac{\kappa_\mathrm{v}\kappa_\mathrm{i}P^\star}{3CV_\mathrm{eq}^2} \\ \frac{\sqrt{2}E\cos\delta_\mathrm{eq}}{L_\mathrm{f}} & -\frac{\kappa_\mathrm{v}\kappa_\mathrm{i} i_{\mathrm{d,eq}}^2}{\sqrt{2}CV_\mathrm{eq}^2} + \frac{2\kappa_\mathrm{v}\kappa_\mathrm{i} i_{\mathrm{d,eq}}P^\star}{3CV_\mathrm{eq}^3} & -\omega_\mathrm{nom} + \frac{\sqrt{2}\kappa_\mathrm{v}\kappa_\mathrm{i} i_{\mathrm{d,eq}}}{CV_\mathrm{eq}} - \frac{\kappa_\mathrm{v}\kappa_\mathrm{i}P^\star}{3CV_\mathrm{eq}^2} & -\frac{R_\mathrm{f}}{L_\mathrm{f}} \end{bmatrix}$
Droop	$\begin{bmatrix} 0 & 0 & 0 & 0 & -m_\mathrm{p} \\ 0 & -\omega_\mathrm{c} + \frac{3}{\sqrt{2}}m_\mathrm{q}\omega_\mathrm{c} i_{\mathrm{q,eq}} & 0 & \frac{3}{\sqrt{2}}m_\mathrm{q}\omega_\mathrm{c}V_\mathrm{eq} & 0 \\ \frac{\sqrt{2}E\sin\delta_\mathrm{eq}}{L_\mathrm{f}} & \frac{\sqrt{2}}{L_\mathrm{f}} & -\frac{R_\mathrm{f}}{L_\mathrm{f}} & \omega_\mathrm{nom} - m_\mathrm{p}(\overline{P}_\mathrm{eq} - P^\star) & -m_\mathrm{p} i_{\mathrm{q,eq}} \\ \frac{\sqrt{2}E\cos\delta_\mathrm{eq}}{L_\mathrm{f}} & 0 & -\omega_\mathrm{nom} + m_\mathrm{p}(\overline{P}_\mathrm{eq} - P^\star) & -\frac{R_\mathrm{f}}{L_\mathrm{f}} & m_\mathrm{p} i_{\mathrm{d,eq}} \\ 0 & \frac{3}{\sqrt{2}}\omega_\mathrm{c} i_{\mathrm{d,eq}} & \frac{3}{\sqrt{2}}\omega_\mathrm{c}V_\mathrm{eq} & 0 & -\omega_\mathrm{c} \end{bmatrix}$

line dynamics and the controller dynamics. Before examining the two GFM controller types individually, we note that the equilibria, $i_{\mathrm{d,eq}}, i_{\mathrm{q,eq}}$ corresponding to the line dynamics in (2) are given by the solution of:

$$-\frac{R_\mathrm{f}}{L_\mathrm{f}} i_{\mathrm{d,eq}} + \omega_\mathrm{i} i_{\mathrm{q,eq}} + \frac{\sqrt{2}}{L_\mathrm{f}}(V_\mathrm{eq} - E\cos\delta_\mathrm{eq}) = 0, \quad (14a)$$

$$-\frac{R_\mathrm{f}}{L_\mathrm{f}} i_{\mathrm{q,eq}} - \omega_\mathrm{i} i_{\mathrm{d,eq}} + \frac{\sqrt{2}}{L_\mathrm{f}}(E\sin\delta_\mathrm{eq}) = 0, \quad (14b)$$

where $V_\mathrm{eq}, \delta_\mathrm{eq}$ are the terminal voltage amplitude and phase-angle equilibria. In what follows, we analyze the AHO and droop controller dynamics in steady state. This will tease out the requisite algebraic equations—that alongside (14a)–(14b)—facilitate the solution for $V_\mathrm{eq}, \delta_\mathrm{eq}, i_{\mathrm{d,eq}}, i_{\mathrm{q,eq}}$. (Droop control involves additional states attributed to the low-pass power filters.) Small-signal dynamic models are then obtained by linearizing the original models around the equilibria.

A. AHO Controller

To obtain the full set of equilibria, we set $\dot{V} = 0$ and $\dot{\delta} = 0$ in (8a) and (9). This yields the following algebraic equations

$$\frac{2\xi}{\kappa_\mathrm{v}^2} V_\mathrm{eq}\left(V_\mathrm{nom}^2 - V_\mathrm{eq}^2\right) + \frac{\kappa_\mathrm{v}\kappa_\mathrm{i}}{3CV_\mathrm{eq}}\left(\frac{3}{2}\sqrt{2}V_\mathrm{eq} i_{\mathrm{q,eq}} + Q^\star\right) = 0 \quad (15a)$$

$$\omega_\mathrm{nom} - \omega_\mathrm{e} - \frac{\kappa_\mathrm{v}\kappa_\mathrm{i}}{3CV_\mathrm{eq}^2}\left(\frac{3}{2}\sqrt{2}V_\mathrm{eq} i_{\mathrm{d,eq}} - P^\star\right) = 0. \quad (15b)$$

Solving (14a), (14b), (15a), and (15b) yields the equilibria: $V_\mathrm{eq}, \delta_\mathrm{eq}, i_{\mathrm{d,eq}}, i_{\mathrm{q,eq}}$. (We refrain from commenting on existence and number of solutions and reserve this for future work.) Introduce the following state variables that capture the dynamics of small perturbations in states of the AHO controller around their equilibria:

$$\Delta\delta = \delta - \delta_\mathrm{eq}, \quad \Delta V = V - V_\mathrm{eq},$$
$$\Delta i_\mathrm{d} = i_\mathrm{d} - i_{\mathrm{d,eq}}, \quad \Delta i_\mathrm{q} = i_\mathrm{q} - i_{\mathrm{q,eq}}.$$

The state vector of the small-signal model is defined as $\Delta x = [\Delta\delta, \Delta V, \Delta i_\mathrm{d}, \Delta i_\mathrm{q}]^\top$. The dynamics of the small-signal model are obtained by linearizing (2), (8a), and (9) around the equilibria. The small-signal model is compactly represented as $\Delta\dot{x} = A\Delta x$, where $A \in \mathbb{R}^{4\times4}$ is the Jacobian matrix of the nonlinear dynamical model evaluated for the equilibria referenced above. The entries of A are reported in Table I.

B. Droop Controller

To obtain the full set of equilibria, we examine (10a), (13), and the active-power filtering dynamics from (11) in steady state. This yields the following algebraic equations:

$$V_\mathrm{eq} - V_\mathrm{nom} - m_\mathrm{q}\left(\frac{3}{2}\sqrt{2}V_\mathrm{eq} i_{\mathrm{q,eq}} + Q^\star\right) = 0, \quad (16a)$$

$$\omega_\mathrm{nom} - \omega_\mathrm{e} - m_\mathrm{p}\left(\overline{P}_\mathrm{eq} - P^\star\right) = 0, \quad (16b)$$

$$\overline{P}_\mathrm{eq} - \frac{3}{2}\sqrt{2}V_\mathrm{eq} i_{\mathrm{d,eq}} = 0. \quad (16c)$$

Solving (14a)–(14b), and (16a)–(16c) yields the equilibria: $V_\mathrm{eq}, \delta_\mathrm{eq}, i_{\mathrm{d,eq}}, i_{\mathrm{q,eq}}, \overline{P}_\mathrm{eq}$. Note that the filtered reactive power is linearly related to the terminal voltage, and therefore, we exclude it in the small-signal model. We introduce the following state variables:

$$\Delta\delta = \delta - \delta_\mathrm{eq}, \quad \Delta V = V - V_\mathrm{eq},$$
$$\Delta i_\mathrm{d} = i_\mathrm{d} - i_{\mathrm{d,eq}}, \quad \Delta i_\mathrm{q} = i_\mathrm{q} - i_{\mathrm{q,eq}}, \quad \Delta\overline{P} = \overline{P} - \overline{P}_\mathrm{eq}.$$

The state vector of the small-signal model is defined as $\Delta x = [\Delta\delta, \Delta V, \Delta i_\mathrm{d}, \Delta i_\mathrm{q}, \Delta\overline{P}]^\top$. The dynamics of the small-signal model are obtained by linearizing (2), (11), (12a), and (13). The small-signal model is compactly represented as $\Delta\dot{x} =$

$A\Delta x$, where $A \in \mathbb{R}^{5\times5}$ is the Jacobian matrix of the nonlinear dynamical model evaluated for the equilibria referenced above. The entries of A are reported in Table I.

IV. Numerical Simulations

We perform numerical simulations to characterize small-signal stability of the AHO and droop controllers leveraging the models in Section III. We begin with the comparison of the transient response between those two controllers. Next, we perform eigen-analysis of the small-signal models while varying the $R_\mathrm{f}/L_\mathrm{f}$ ratio and the active-power setpoint, $P^\star$. Lastly, we validate our analysis by simulating the nonlinear dynamics. The parameters of the controllers are listed in Table II. The detailed procedure to determine the AHO controller parameters is available in [2]. The inverter is assumed to be rated at $S_\mathrm{rated} = 1200$W. For the droop controller, the cut-off frequency of the LP filter is selected to be 30 Hz to filter out the switching ripples and 120 Hz harmonics caused by potential imbalances in the three-phase network.

A. Transient Response Comparison

We consider the case when $R_\mathrm{f}/L_\mathrm{f} = 533.3$ Hz, ($L_\mathrm{f} = 1.5$ mH and $R_\mathrm{f} = 0.8\ \Omega$), $P^\star$ steps up from 0 to 500 W while $Q^\star = 0$ VA. For this case, the eigenvalues of the Jacobian matrix A are plotted in the background of the top pane of Fig. 3. The largest real parts of the eigenvalues are -104 and -57 for AHO and droop controllers, respectively. This tells us that the AHO has faster response than the droop controller. This is validated by the plot of the step response at the front of the top pane of Fig. 3 and the plots of the filter currents at the bottom pane of Fig. 3.

B. Impact of Varying $R_\mathrm{f}/L_\mathrm{f}$ Ratio

The $R_\mathrm{f}/L_\mathrm{f}$ ratio plays a key role in influencing the eigenvalues for the GFM systems. We will show that there is a critical $R_\mathrm{f}/L_\mathrm{f}$ value identifying the stability of both VOC and droop control. We can observe from Fig. 4 that in a purely inductive network ($R_\mathrm{f}/L_\mathrm{f} = 0$), the system is unstable due to two RHS eigenvalues. While increasing $R_\mathrm{f}/L_\mathrm{f}$, we can see that the system becomes stable when $R_\mathrm{f}/L_\mathrm{f} > (R_\mathrm{f}/L_\mathrm{f})_\mathrm{cr}$. We conclude that the filter dynamics play an important role in identifying the stability of such a system.

We swept the value of $R_\mathrm{f}/L_\mathrm{f}$ for AHO and droop control within the same range, and we obtain the eigenvalues as plotted in Fig. 4. We observe that $R_\mathrm{f}/L_\mathrm{f}$ has the following impacts on stability: a small $R_\mathrm{f}/L_\mathrm{f}$ value may cause instability. The critical $R_\mathrm{f}/L_\mathrm{f}$ values for the AHO and droop controllers are: $(R_\mathrm{f}/L_\mathrm{f})_\mathrm{cr,AHO} \approx 180$ Hz and $(R_\mathrm{f}/L_\mathrm{f})_\mathrm{cr,droop} \approx 173$ Hz.

TABLE II
Parameters for the AHO and Droop Controllers.

AHO Controller	Droop Controller
$\kappa_\mathrm{v} = 120$ V, $\kappa_\mathrm{i} = 0.24$ V/W	$m_\mathrm{p} = 2.6 \times 10^{-3}$ V/W
$\xi = 15$ /sV^2	$m_\mathrm{q} = 5.0 \times 10^{-3}$ rad/sVar
$C = 0.2679$ F, $L = 26.268$ μH	$\omega_\mathrm{c} = 2\pi30$ rad/s

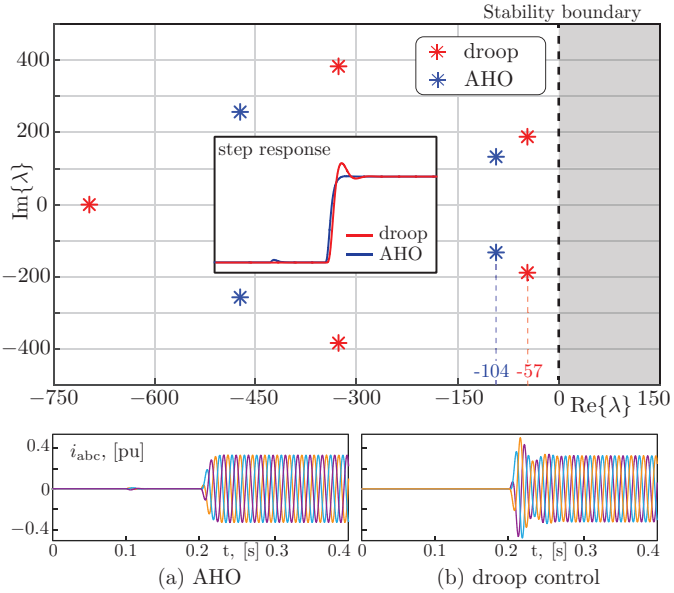

Figure 3: Transient response of AHO and droop controllers.

C. Impact of Varying Active Power Command

From the A matrix, we see that the power setpoint $P^\star$ may have impacts on the locations of eigenvalues to some extent. To investigate this, we sweep $P^\star$ from 0 to 1200 W while keeping $Q^\star = 0$. The eigenvalues are plotted in Fig. 5. From the figure, we can conclude that the eigenvalues change slightly along with the $P^\star$ variation. It implies that the power reference has little impact on small-signal stability.

D. Validation with Nonlinear Dynamical Model

We validate the small-signal models and stability analysis with nonlinear simulations. To this end, we select two $R_\mathrm{f}/L_\mathrm{f}$ values: $R_\mathrm{f}/L_\mathrm{f} = 333.3$ Hz and 133.3 Hz. Figure 6 shows simulations of the terminal voltage amplitude V and angle δ for both cases. We observe that the first case is stable while the second case is not. The results demonstrate agreement with the linearization and stability analysis.

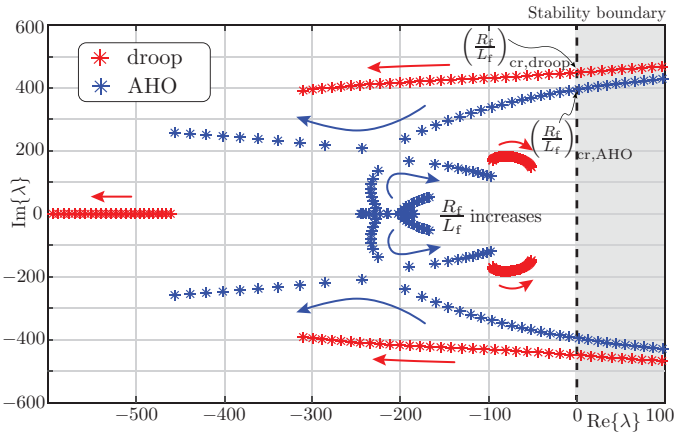

Figure 4: Eigenvalue analysis with different $R_\mathrm{f}/L_\mathrm{f}$ ratios.

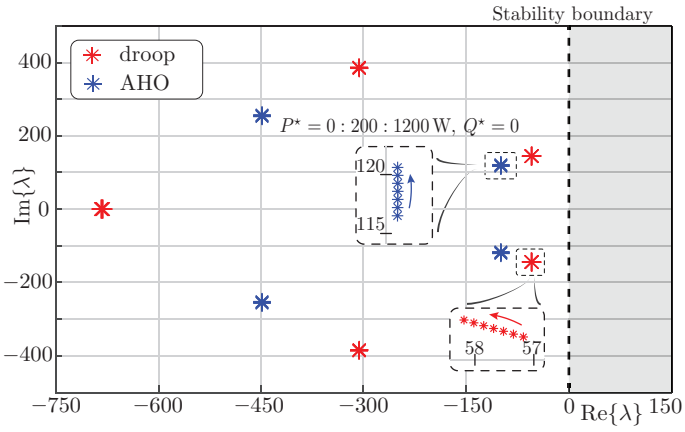

Figure 5: Eigenvalue analysis for active-power setpoints $P^\star = 0 \rightarrow 1200$ W.

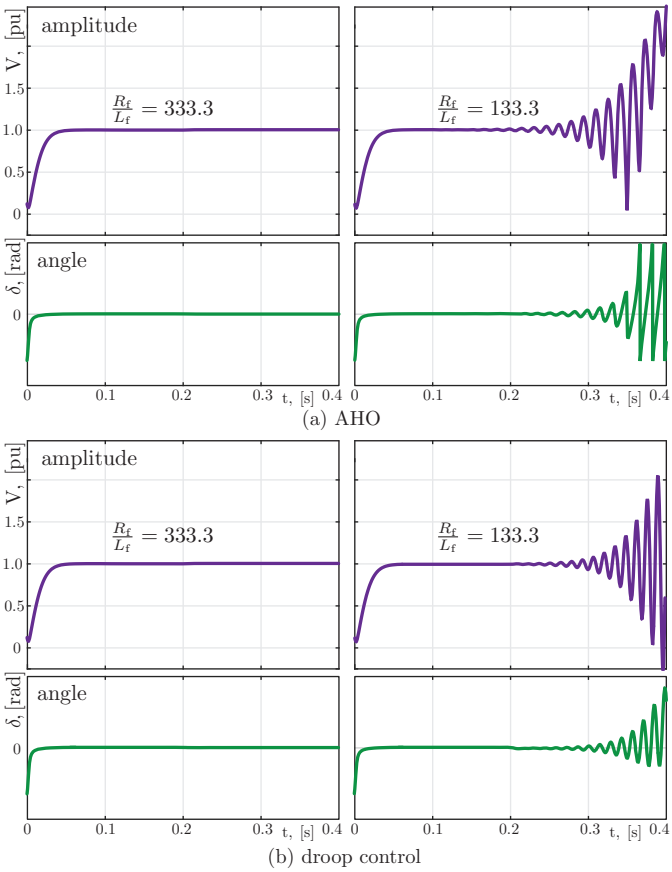

Figure 6: Simulation results of terminal voltage amplitude V and phase-angle δ when $R_f/L_f = 333.3$ Hz and 133.3 Hz for (a) AHO and (b) droop control.

V. Concluding Remarks & Future Work

This paper was focused on a comparative analysis of GFM inverters programmed with Andronov-Hopf oscillator dynamics and droop control. A small-signal model was formulated for a single inverter to infinite bus system for both control types. With this model in hand, the system eigenvalues were studied while sweeping relevant parameters and setpoints. These models were then validated via nonlinear time-domain simulations. Future work will be focused on characterizing the existence and uniqueness of the system equilibria as well as experimental validations on inverter hardware.

References

[1] Y. Kuznetsov, *Elements of Applied Bifurcation Theory*. Springer-Verlag New York, 2004.

[2] M. Lu, S. Dutta, V. Purba, S. Dhople, and B. Johnson, "A grid-compatible virtual oscillator controller: Analysis and design," in *IEEE Energy Conversion Congress and Exposition*, pp. 2643–2649, Sep. 2019.

[3] S. V. Dhople, B. B. Johnson, and A. O. Hamadeh, "Virtual oscillator control for voltage source inverters," in *51st Annual Allerton Conference on Communication, Control, and Computing*, pp. 1359–1363, Oct. 2013.

[4] B. Johnson, M. Sinha, N. Ainsworth, F. Dörfler, and S. Dhople, "Synthesizing Virtual Oscillators to Control Islanded Inverters," *IEEE Trans. Power Electron.*, vol. 31, pp. 6002–6015, Aug. 2016.

[5] D. Raisz, T. T. Thai, and A. Monti, "Power control of virtual oscillator controlled inverters in grid-connected mode," *IEEE Trans. Power Electron.*, vol. 34, pp. 5916–5926, Jun. 2019.

[6] B. B. Johnson, S. V. Dhople, A. O. Hamadeh, and P. T. Krein, "Synchronization of Nonlinear Oscillators in an LTI Electrical Power Network," *IEEE Transactions on Circuits and Systems I: Regular Papers*, vol. 61, pp. 834–844, Mar. 2014.

[7] L. A. B. Tôrres, J. P. Hespanha, and J. Moehlis, "Power supplies dynamical synchronization without communication," in *2012 IEEE Power and Energy Society General Meeting*, Jul. 2012.

[8] M. C. Chandorkar, D. M. Divan, and R. Adapa, "Control of parallel connected inverters in standalone AC supply systems," *IEEE Trans. Ind. Appl.*, vol. 29, pp. 136–143, Jan. 1993.

[9] J. M. Guerrero, J. C. Vasquez, J. Matas, L. G. de Vicuña, and M. Castilla, "Hierarchical control of droop-controlled AC and DC microgrids–a general approach toward standardization," *IEEE Trans. Ind. Electron.*, vol. 58, no. 1, pp. 158–172, 2011.

[10] Y. Sun, X. Hou, J. Yang, H. Han, M. Su, and J. M. Guerrero, "New perspectives on droop control in AC microgrid," *IEEE Trans. Ind. Electron.*, vol. 64, pp. 5741–5745, Jul. 2017.

[11] N. Pogaku, M. Prodanovic, and T. C. Green, "Modeling, Analysis and Testing of Autonomous Operation of an Inverter-Based Microgrid," *IEEE Trans. Power Electron.*, vol. 22, pp. 613–625, Mar. 2007.

[12] N. Bottrell, M. Prodanovic, and T. C. Green, "Dynamic stability of a microgrid with an active load," *IEEE Trans. Power Electron.*, vol. 28, pp. 5107–5119, Nov. 2013.

[13] K. Yu, Q. Ai, S. Wang, J. Ni, and T. Lv, "Analysis and optimization of droop controller for microgrid system based on small-signal dynamic model," *IEEE Trans. Smart Grid*, vol. 7, pp. 695–705, Mar. 2016.

[14] X. Guo, Z. Lu, B. Wang, X. Sun, L. Wang, and J. M. Guerrero, "Dynamic phasors-based modeling and stability analysis of droop-controlled inverters for microgrid applications," *IEEE Trans. Smart Grid*, vol. 5, pp. 2980–2987, Nov. 2014.

[15] M. Sinha, F. Dörfler, B. B. Johnson, and S. V. Dhople, "Uncovering droop control laws embedded within the nonlinear dynamics of Van der Pol oscillators," *IEEE Control Netw. Syst.*, vol. 4, pp. 347–358, Jun. 2017.

[16] Z. Shi, J. Li, H. Nurdin, and J. E. Fletcher, "Comparison of virtual oscillator and droop controlled islanded three-phase microgrids," *IEEE Trans. Energy Convers.*, pp. 1–1, 2019.

[17] B. Johnson, M. Rodriguez, M. Sinha, and S. Dhople, "Comparison of virtual oscillator and droop control," in *Workshop on Control and Modeling for Power Electronics*, 2017.

[18] G. Seo, M. Colombino, I. Subotic, B. Johnson, D. Groß, and F. Dörfler, "Dispatchable virtual oscillator control for decentralized inverter-dominated power systems: Analysis and experiments," in *IEEE Applied Power Electronics Conference and Exposition*, pp. 561–566, Mar. 2019.

[19] M. Colombino, D. Gross, J. Brouillon, and F. Dörfler, "Global phase and magnitude synchronization of coupled oscillators with application to the control of grid-forming power inverters," *IEEE Trans. Autom. Control*, pp. 1–1, 2019.

[20] D. Groß, M. Colombino, J. Brouillon, and F. Dörfler, "The effect of transmission-line dynamics on grid-forming dispatchable virtual oscillator control," *IEEE Control of Netw. Syst.*, vol. 6, pp. 1148–1160, Sep. 2019.

[21] A. Yazdani and R. Iravani, *Voltage-Sourced Converters in Power Systems*. Hoboken, NJ: John Wiley & Sons, Inc., 2010.